IEEE Geosci. Remote Sensing Symp, Seattle, July 1998

3-D Simulation Of Subsurface PEC Sensing For Discimination Enhancement Using Bistatic Positional, Angular, and Polarization Diversity

Shah A. Haider[+], Kevin O'Neill[#], and Keith D. Paulsen[+]

[+]Thayer School of Engineering, Dartmouth College, Hanover NH 03755 USA
Shah.A.Haider@Dartmouth.edu, Keith.D.Paulsen@Dartmouth.edu

[#]US Army Cold Regions Research and Engineering Laboratory, 72 Lyme Rd, Hanover NH 03755 USA
koneill@crrel.usace.army.mil

ABSTRACT

This paper presents results intended to improve our understanding of the gains to be made in subsurface electromagnetic discrimination by employing bistatic positional, angular, and polarization diversity. Applying a 3-D finite element approach eliminates any restriction to axisymmetric geometries in targets and environment; and recent numerical innovations allow us to perform meaningful 3-D simulations at the workstation level. For specificity we assume an incident wave polarized in the (X,Z) plane of incidence, where Z is aligned with longitudinal target axis, for orientable targets. The simulations show physically explicable gains in discrimination from bistatic, polarimetric, multi-angle observation, even at a single frequency with wavelengths an order of magnitude larger than characteristic target dimensions.

INTRODUCTION

It has been reported that over 11,000,000 acres in the US that are potentially contaminated by UXO [1]. The need for clean up has lent urgency to the quest for effective discrimination of subsurface objects. Measurement results that are just appearing in the low frequency broadband induction realm [2] suggest that different metallic objects on the size scale of UXO display distinct behaviors despite the enormous incident wavelength relative to object dimensions. This contradicts our tendency to regard small "particles" as more or less isotropic Rayleigh scatterers, with little in their scattering behavior that distinguishes one geometry from another.

In the simulations reported here, as in field surveying, low frequencies are chosen because they are unhindered by possible soil lossiness which can confound even shallow subsurface sensing at higher frequencies, depending upon conditions. The objects are assumed to be contained in an infinite medium of relative dielectric constant 9, typical of moist soil. Because the frequencies are low and sensing is very shallow we neglect conductive losses, though that can easily be included. To isolate the effect of target morphology, we hold the object volume constant while varying shape, considering a sphere of radius a, a cube of side h, cylinders of diameter D and lengths l equal to D or $3D$. Results from other shapes including flattened cubes, shorter and longer cylinders, and various spheroids, with broader band illumination, will be reported elsewhere. Here, with a fixed volume of 1/16 m^3, the target dimensions vary from a cube with $l \sim 0.4$ m, a sphere with $a \sim 0.25$ m, an "equi-dimensional" or "short" 1×1 cylinder with $l = D \sim 0.27$ m, and an elongated cylinder 1×3 cylinder with $D = 0.188$ m and $l = 0.563$ m.

For specificity we perform all simulations at a frequency of 30 MHz At the bottom of the GPR range, this frequency is low enough so that medium lossiness should not be a problem, especially in shallow (e.g. UXO) sensing. However it entails the limitation that the wavelength is an order of magnitude greater than the typical target dimensions. To avoid limiting the results to any particular sensor apparatus and to retain the focus on basic object scattering properties, the incident beam is assumed to be a plane wave. It impinges at various dictated angles relative to the positive Z axis, which coincides with the longitudinal axis of those targets that are orientable. The target is centered at the

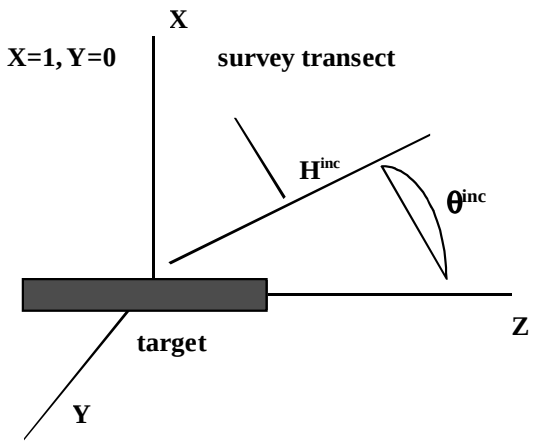

Figure 1. Coordinate, incidence, and target orientations.

origin, and bistatic scattering results are obtained along a hypothetical survey transect 1 m above the target, i.e. at X = 1. Incident illumination is in the (X,Z) plane, and we restrict ourselves here to the incident polarization shown in Fig 1 ($E_y = 0$; $H_z = 0$).

SIMULATION APPROACH

The ultimate source of the algebraic numerical equations is Maxwell's curl equations, with a modification to include Gauss's law for magnetic fields.

$$\nabla \times \frac{i}{\omega\varepsilon}\nabla \times \mathbf{H} - \nabla\left[\frac{i}{\omega\mu\varepsilon}\nabla \cdot \mu\mathbf{H}\right] - i\omega\mu\mathbf{H} \;=\; 0 \qquad (1)$$

where ω is the circular frequency, μ is the medium permeability, ε the complex permittivity, and **H** the magnetic field. We have included the second term, expressing the divergence- free character of the associated **B** field, to insure against the numerical development of non-physical, spurious modes in the solutions [3,4,5]. When this equation is multiplied by a weighting function $\varphi_i(r)$, then integrated over the domain and vector integral identities are applied, the required weak form results:

$$\left\langle\left(\frac{1}{i\omega\varepsilon}\nabla \times \mathbf{H}\right) \times \nabla\varphi_i\right\rangle + \left\langle\frac{1}{i\omega\mu\varepsilon}(\nabla \cdot \mu\mathbf{H})\nabla\varphi_i\right\rangle + \langle i\omega\mu\mathbf{H}\varphi_i\rangle$$
$$= \oint dS(\hat{\mathbf{n}} \times \mathbf{E})\varphi_i \;+\; \oint dS\hat{\mathbf{n}}\left(\frac{1}{i\omega\mu\varepsilon}(\nabla \cdot \mu\mathbf{H})\right)\varphi_i \qquad (2)$$

where the brackets <...> denote spatial integration over the entire solution domain and the integrations on the right hand side are performed over the surface of that domain. To achieve our finite element formulation we approximate H as the summation $\sum H_j\varphi_j(r)$, where the nodal values H_j are to be determined. Each $\varphi_j(r)$ is a basis function that serves to perform a 3-D piecewise linear interpolation of **H** between nearby nodes. Thus the weighting and basis functions form the same set. This selection of the Galerkin finite element approach provides maximum flexibility in treating arbitrary target and environmental geometry.

While details of the formulation are provided elsewhere [eg references above], a few key points follow here. First, we note that we have chosen this form because it allows us to specify known source excitation easily. For our pec targets, the target interior is outside the solution domain, thus the first integral on the right hand side of (2) includes its surface. We solve only for the *scattered* fields. Given a known incident field $\mathbf{E}^{inc}$, we drive the system by specifying $\hat{\mathbf{n}} \times \mathbf{E}$ in the integral as the negative of $\hat{\mathbf{n}} \times \mathbf{E}^{inc}$. The target surface becomes in effect an inner surface and source, located at the center of our numerical domain. Choosing the H field formulation also has the advantage that dielectric discontinuities in the domain do not impose H field discontinuities which would require special treatment.

We must still treat the outer surface of the finite discretization, which for economy's sake we want to locate as near as possible to the target without disturbing its response. This is accomplished with an perfectly matched layer (PML) on the exterior of the domain of interest. Within the PML the medium is considered anisotropic

$$\mathbf{D} = \varepsilon\Lambda \cdot \mathbf{E}, \quad \mathbf{B} = \mu\Lambda \cdot \mathbf{H} \qquad (3)$$

The diagonal tensor Λ has generally unequalcomplex elements a_1, a_2, a_3, which take on special relationships in the absorbing layer to preserve the perfect match with the domain interior [6,7,8]. The anisotropicity allows the layer to extinguish waves propagating into the outer boundary from any interior direction. Equation (1) may be recast using (3), yielding.

$$\nabla \times \frac{i}{\omega\varepsilon}\Lambda^{-1} \cdot \nabla \times \mathbf{H} + \Lambda \cdot \nabla\left[\frac{i}{\omega\mu\varepsilon a_1 a_2 a_3}\nabla \cdot \mu\mathbf{H}\right] - i\omega\mu\Lambda \cdot \mathbf{H} \;=\; 0 \qquad (4)$$

Material dependent basis functions within the PML also solve implementation of essential continuity and uniqueness conditions. The particular formulation chosen may then be discretized in the same manner as led to (2) above, retaining many of the desirable features of isotropic cases, such as matrix symmetry. Overall, the program distinguishes itself in implementing an anisotropic PML with nodal based finite elements, using a spurious solution free modified form of the vec-

tor Helmholtz equation. The ultimate result allows very large efficiencies in terms of diminished mesh requirements. While we have used rectilinear mesh terminations for the results reported here, the method itself is not subject to that restriction.

RESULTS

Fig 2 shows $|H_y|$ values along the transect line parallel to Z for normal ($\theta^{inc} = 90^0$) incidence at 30 MHz. In this and all subsequent cases, we assume a unit incident magnitude E field, thus the incident H magnitude is about 10^{-3} A/m.

The elongated cylinder produces the strongest response, followed by the shorter cylinder, sphere, and lastly the cube. Overall, under a considerable variety of conditions not shown here, the cube produces the weakest response of all the shapes, for a given material volume. The incident field tends to induce Z-directed dipolar current configurations in the targets. We note that the relatively elongated cylinder is the most effective re-radiator because currents on its surface most easily align coherently, in this case predominantly parallel to the Z axis. For an infinite pec cylinder subjected to oblique incidence with this polarization, in fact we expect *only* Z-directed surface currents, despite possibly strong E_x components in the incident field [9].

Fig 3 shows bistatic $|H_y|$ results along the same line, at 30^0 incidence. In this instance, most of the target responses can be distinguished from one another by their *shapes* as well as magnitudes.

The elongated cylinder response is most nearly centered about Z = 0. This is because its surface current pattern most nearly forms an electric dipole but has little phase variation along its length. For more elongated

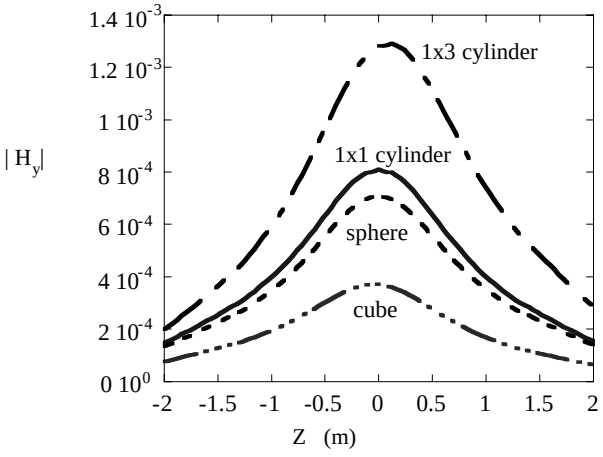

Figure 2. Patterns of $|H_y|$ at 30 MHz along X = 1, Y = 0 at normal (90°) incidence.

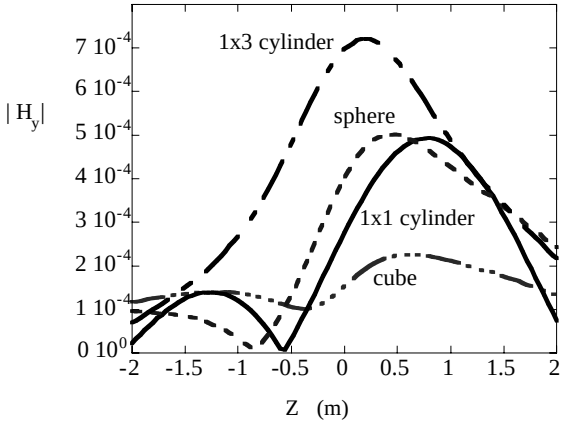

Figure 3. Scattered $|H_y|$ values for cube, sphere, and cylinders at 30 MHz, 30° incidence.

cylinders (eg 1×9 such that $l \sim \lambda$, and longer cases) we see the scattering peak shift more towards the specular direction (Z ~ –1.2 m). .Here all of the other targets produce a lobe at least somewhat shifted towards the incidence direction. The relatively weak cube response is by far least varied in magntiude along the transect. The great similarity in patterns from the sphere and short cylinder indicate that the prominent flat ends of the latter do not play a significant in this instance, despite the angle of incidence. The completely faceted cube produces a proportionally greatest amount of forward scatter.

The cube and short cylinder show similar responses in other instances and views, and are generally the hardest two cases to distinguish based on their responses. For example, in the same case run about three orders of magnitude lower in frequency (25 kHz), the $\mathrm{Im}\{H_y\}$ components dominates and shows a very similar pattern and relationship. Remaining with 30 MHz, bistatic information in the E field components and in diverse H components seen from other positions help resolve ambiguities between sphere and short cylnder response. Fig 4 shows all H component results for the same cases, with $\theta^{inc} = 30^0$, but along the line X=1, Z=0, $-2 < Y < 2$, thus, along a line orthogonal to the previous transect.

The field patterns all show evidence of strong induced currents in the Z direction, despite the oblique incidence. The cube is distinctly the weakest re-radiator, and its scattered $|H_y|$ component is not very strikingly dominant. $|H_y|$ is comparably increased in both the sphere and short cylinder cases, however in the latter case the significance of $|H_x|$ is about the same as that of $|H_z|$. This greater $|H_x|$ significance from the short cylinder is because, despite its eggregiously flattened ends and short barrel relative to the wavelenth ($l/\lambda <$ 0.1), the induced currents on the barrel still tend to line

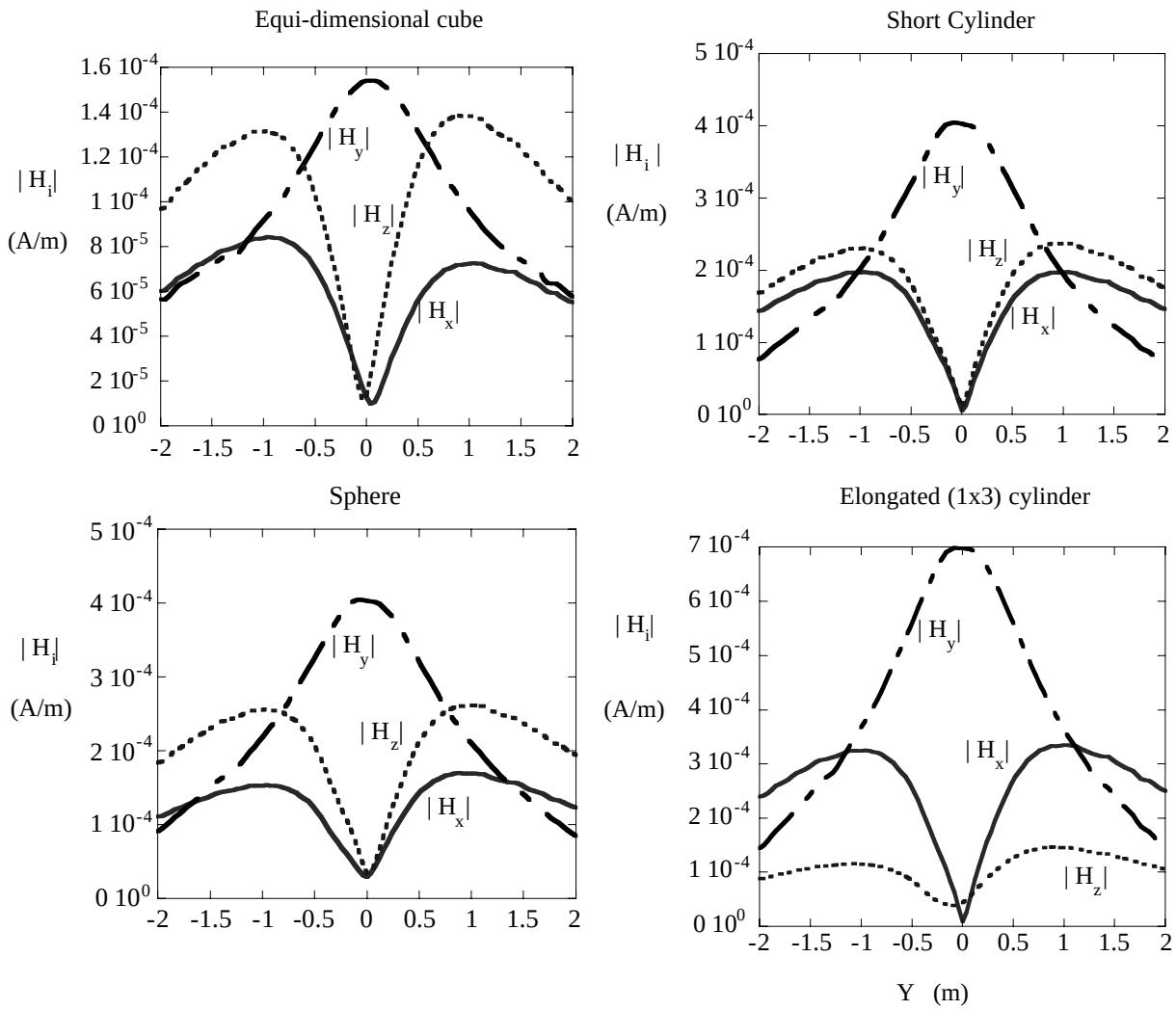

Figure 4. H component response along line X = 1, Z = 0 –2 < Y < 2, for four target geometries.

up somewhat in the manner expected in a long cylinder (cf 1×3 cylinder pattern). The scattered $|H_z|$ patterns are consistent with vertical (X-directed) currents, which decline in significance as the target is more cylindrical and more elongated. These inferences are supported by examination of the corresponding scattered E fields, not shown. In general the patterns in Fig 5 and their E field counterparts are *not* consisent with assuming current loops induced on the targets.

CONCLUSION

Three-D finite element simulations show their benefits in simulating bistatic positional, angular, and polarization diversity for discrimination of metallic shapes embedded in a dielectric. The method freely treats arbitrary shapes beyond the capabilities of BOR programs, and an anisotropic PML effectively absorbs unwanted mesh boundary reflections extremely effectively. The results show distinctive scattering responses by different target shapes, which can generally be related to logical current patterns induced on the contrasting morphologies. This is true despite an incident wavelength approximately an order of magnitude larger than typical target dimensions, as is often necessarily the case for radar to penetrate the ground. Ongoing work focuses on broadband and time domain simulation, from the audio frequency electromagnetic induction realm through GPR frequencies in the 100's of MHz, where possible still utilizing the diversity of factors varied here..

REFERENCES

[1]. B. Johnson, T.G. Moore, B.J. Blejer, C.F. Lee, T.P. Opar, S. Ayasli, and C.A. Primmerman, A Research and Development Strategy for Unexploded Ordnance Sensing, Lincoln Laboratory Project Report PR-EMP-1, 144pp, 1996.

[2]. E.I. Novikova, I.J. Won, and A. Witten, Subsurface Imaging with Broadband Electromagnetic Induction, Phillips Laboratory Report PL-TR-97-2142, Hanscom AFB, MA, 79pp., 1997.

[3]. K.D. Paulsen and D.R. Lynch, "Elimination of Vector Parasites in Finite Element Maxwell Solutions", IEEE Trans. MTT, vol 39, pp.395-404, 1991.

[4] .W.E. Boyse, D.R. Lynch, and K.D. Paulsen, G.N. Minerbo, "Nodal Based Finite Element Modeling of Maxwell's Equations in Three Dimensions", IEEE Trans. AP, vol 40(6), pp.642-651, 1992.

[5]. K.D. Paulsen, "Finite element solution of Maxwell's equations with Helmholtz forms",J. Opt. Soc. Am. A: Special Issue on Scattering by Three-dimensional Objects, vol 11. pp.1434-1444, 1994.

[6]. Z. S. Sacks, D. M. Kingsland, R. Lee and J-F Lee, "A perfectly matched anisotropic absorber for use as an absorbing boundary condition," IEEE Trans. AP, vol 43(12), pp.1460-63,1995.

[7]. J-Y Wu, D.M. Kingsland, J-F Lee, and R. Lee, "A Comparison of Anisotropic PML to Brenger's PML and Its Application to the Finite-Element Method for EM Scattering," IEEE Trans. AP, vol. 45(1), pp.45-50,1997.

[8]. J. Tang, K.D. Paulsen, and S.A. Haider, "Perfectly matched layer mesh terminations for nodal-based finite element methods in electromagnetic scattering," IEEE Trans AP, (in press), 1998.

[9]. J.R. Wait, "Scattering of a plane wave from a circular dielectric cylinder at oblique incidence," Can. J. Phys., vol 33, pp.189-195, 1955.